Characterization of period-doubling scenarios in Taylor-Couette flow

Th. Buzug, J. von Stamm, and G. Pfister

Institut für Angewandte Physik, Christian Albrechts Universität zu Kiel, W-2300 Kiel, Germany

(Received 4 August 1992)

The Taylor-Couette system is an extraordinary hydrodynamic system, showing almost all low-dimensional scenarios for routes to chaos for proper boundary conditions. For a period-doubling route to chaos, bifurcation diagrams were experimentally recorded and the dynamic variables such as fractal dimensions, Lyapunov exponents, and entropies are estimated as a function of Reynolds number. The evolution of the correlation dimension D_2 with Reynolds number Re shows that $D_2 \propto (\text{Re}-\text{Re}_c)^{1/4}$, which is similar to continuous phase transitions. An investigation of the critical phenomena must be performed as high-precision hydrodynamic experiments because the results show that the kind of scenario depends sensitively on the boundary conditions.

PACS number(s): 47.20.−k, 05.45.+b

I. INTRODUCTION

When, in Taylor-Couette flow, the Reynolds number, defined as $\text{Re}=\Omega d r_i /v$, where Ω is the angular frequency of the rotation for the inner cylinder and $d=r_0-r_i$ is the width of the annular gap, is increased gradually starting from zero, the system passes through sequences of space- and time-periodic flow patterns. These scenarios depend sensitively on the boundary conditions and lead finally to chaotic and turbulent motion. Investigations yield a breakup of a two-torus, period doublings, intermittency, homoclinic orbits, and stable three-tori [1–9]. A review of hydrodynamic instabilities is given by Di Prima and Swinney [10]. The importance of the influence of the boundary conditions on the flow was first demonstrated by Benjamin and Mullin [11].

One point of our work is to find functional dependencies of the scenarios on the boundary conditions, so that one may better understand why the solutions of Navier-Stokes equations map onto the solutions of very different low-dimensional models, even if these solutions lie in close proximity in parameter space. This includes slight variations in symmetry to estimate this effect.

The Taylor-Couette experiment considered here concerns the behavior of a flow of a viscous fluid between two concentric cylinders. The outer cylinder, as well as the bottom and top plate, are fixed while the inner one rotates.

The experiments done here are performed in a Taylor-Couette flow with gap-length-to-width ratios ($\Gamma=l/d$) ranging from 0.3 to 0.5, where the solution branches are well known for radius ratio $\eta=0.5$ [12]. The advantage of working with small geometries stems from the fact that the number of solutions is small and that the experiment can be properly controlled. Of particular interest here is a restabilized symmetric two-vortex state which shows various kinds of period multiples as a function of slight changes in the boundary conditions. Results of a period-doubling cascade have been reported in [2,13].

The main concern of this paper is period-multiplying scenarios found in many experimental situations [14–16],

especially period-doubling cascades. In this context we want to give quantitative estimates of the onset of chaos in terms of dynamic variables such as Lyapunov spectra, fractal dimensions, and entropies, and we want to characterize these transitions similar to bifurcations and phase transitions. This paper briefly describes the experimental setup and the bifurcations studied, provides an overview of the methods used to determine the dynamic variables, and then discusses the results obtained from period-multiplying scenarios in terms of the dynamic variables.

II. EXPERIMENTAL SETUP

The Taylor-Couette apparatus used in these experiments consists of a rotating inner cylinder machined from stainless steel having a radius of $r_i=12.5$ mm, a stationary outer cylinder made from optical polished glass with a radius of $r_0=25$ mm, and stationary bottom and top plates. The accuracy of the radii is better than 0.01 mm over the entire length of 220 mm. The length of the cylinder can be varied continuously, so the aspect ratio Γ used as a geometrical control parameter (defined as the ratio of gap length to gap width) takes values from 0 to 17.6. The second geometrical parameter is illustrated in Fig. 1. To get non-cylinder-symmetric boundary conditions the top plate of the apparatus can be inclined by a small amount. As a measure for the inclination we give the parameter k yielding an inclination angle $\varphi=\arctan(k/49.5\text{ mm})$. Silicon oil with different viscosities depending on the flow situation is used as a working fluid. The external control parameter is the Reynolds number defined as $\text{Re}=(\Omega d r_i)/v$, where Ω is the angular frequency of the rotating inner cylinder, $d=r_0-r_i$ the gap width, and v the kinematic viscosity of the oil. The temperature of the fluid is held constant to within 0.01 K by circulating thermostatically controlled silicon oil. The control of the inner cylinder speed is better than one part in 10^{-4} in the short term and better than one part in 10^{-6} in the long-term average. Thus the accuracy of the absolute value of the Reynolds number is about 1% and for relative values better than 10^{-5}. The local velocity is
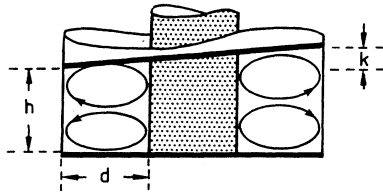
FIG. 1. Sketch of the boundary conditions of the Taylor-Couette system. h, gap length; d, gap width $(\Gamma = h/d)$; k, inclination of top plate.

measured by a real-fringe laser-Doppler velocity meter (LDV) and recorded by a phase-locked-loop (PLL) analog tracker. After filtering by an analog Bessel filter of fourth order, the velocity signal is fed into an analog-to-digital converter (ADC) with a 12-bit resolution and then into a computer where the data processing is performed. For more details of the experimental setup see [13,17,18].

III. BIFURCATIONS

The underlying basic flows considered here are either a symmetric two-vortex state or a single-vortex state with two possible directions of rotation. Figure 2 shows schematically the flow pattern of these two types of flow occurring at an aspect ratio $\Gamma = 0.42$ and $\text{Re} = 550$, drawn after flow visualization photography. (s_1^*) marks the symmetric two-vortex state, (a) an asymmetric single-vortex state (i, inner cylinder; o, outer cylinder). The two-cell flow is mirror symmetric relative to the midplane, so the axial velocity component in this plane is zero for all Reynolds numbers. The single-cell flow appears in two equivalent modes with one big vortex and a small weak one near the bottom or the top plate, respectively, having contrary direction of rotation. So in contrast to the symmetric mode, the axial velocity component is nonzero almost everywhere in the midplane. Thus the location of the LDV measurement volume indicated by X in Fig. 2 is suitable to characterize the actual flow mode by the measurement of the axial velocity component.

Figure 3 shows a bifurcation diagram recorded at an aspect ratio of $\Gamma = 0.374$ and an inclination of the top plate of $k = 0.20$ mm (0.23°). The Reynolds number was scanned quasistatically from $\text{Re} = 50 - 1000$ $(\Delta \text{Re}/\Delta t = 0.04 \text{ s}^{-1})$. The symmetric two-vortex state (s) bifurcates at point A to a single-vortex branch $(a_1$ and a_1^* for different directions of rotation). Branch a_1^* is disconnected by the asymmetry introduced by the inclination of the top plate. The one-vortex state undergoes a Hopf bifur-
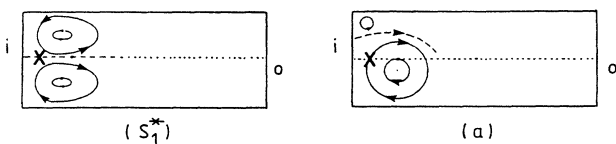

FIG. 2. Flow patterns for the symmetric and asymmetric vortex state. X marks the position of the velocity measurement.
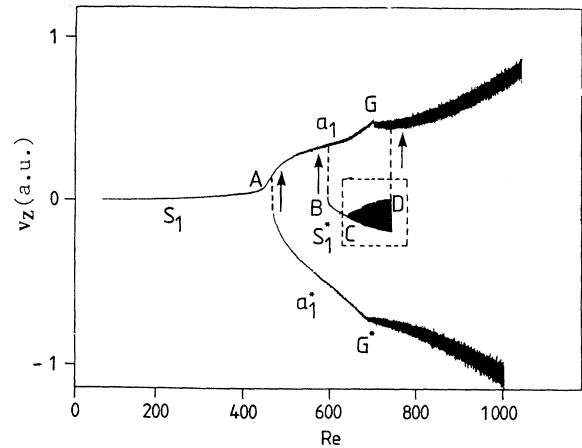

FIG. 3. Bifurcation diagram for $\Gamma = 0.374$ and $k = 0.20$ mm (0.23°). The dashed box indicates the restabilized symmetric state s_1^*.

cation at point G (G^*). The two-vortex state restabilizes at point B, starting a secondary symmetric branch s_1^*. This branch can be reached experimentally by a sudden change in Reynolds number only. Towards higher Reynolds numbers it shows a Hopf bifurcation at point C, which can either show a period-doubling cascade, intermittency, breakup of tori, or odd multiples of the main period, depending on slight changes in aspect ratio or slight inclination of the top plate to reduce symmetry. At point D this state loses stability due to the amplitude of the oscillation and stabilizes into one of the single-vortex states (marked with an arrow). All branches marked with an asterisk are disconnected from the primary solution.

In Figs. 4(a)–4(j) the bifurcation cascades to the chaotic regime are shown for the restabilized symmetric branch (marked with a dashed box in Fig. 3). Here only the successive extrema of the axial velocity v_z are plotted while the Reynolds number is ramped quasistatically. This reveals period doublings and periodic windows in the chaotic regime which are hidden in Fig. 3. The diagrams are drawn for increasing inclination of the top plate k and constant $\Gamma = 0.374$. The maximum inclination in this sequence is $k = 0.36$ mm, corresponding to an angle of 0.42°. One sees the strong dependence of the bifurcation diagram on the boundary conditions. Periodic windows indicated by W_j $(j = 1, 2)$ appear and disappear for certain values of inclination k. The onset of the first Hopf bifurcation to period 1 (marked with P_1) as well as the period-doubling points to periods 2 and 4 $(P_2$ and $P_4)$ are shifted. For $k = 0.3$ mm (0.35°) one obtains a sequence of period-1 oscillations marked with P_1^1, P_1^2, and P_1^3, respectively. The onset of chaos and the length of the chaotic regimes are influenced by the inclination. At the end of each route, the symmetric flow s_1^* becomes unstable and the asymmetric flow appears.

Table I shows the values measured experimentally for the scaling number δ^* obtained from

$$\delta^* = \frac{\text{Re}_j - \text{Re}_{j-1}}{\text{Re}_{j+1} - \text{Re}_j}, \tag{1}$$
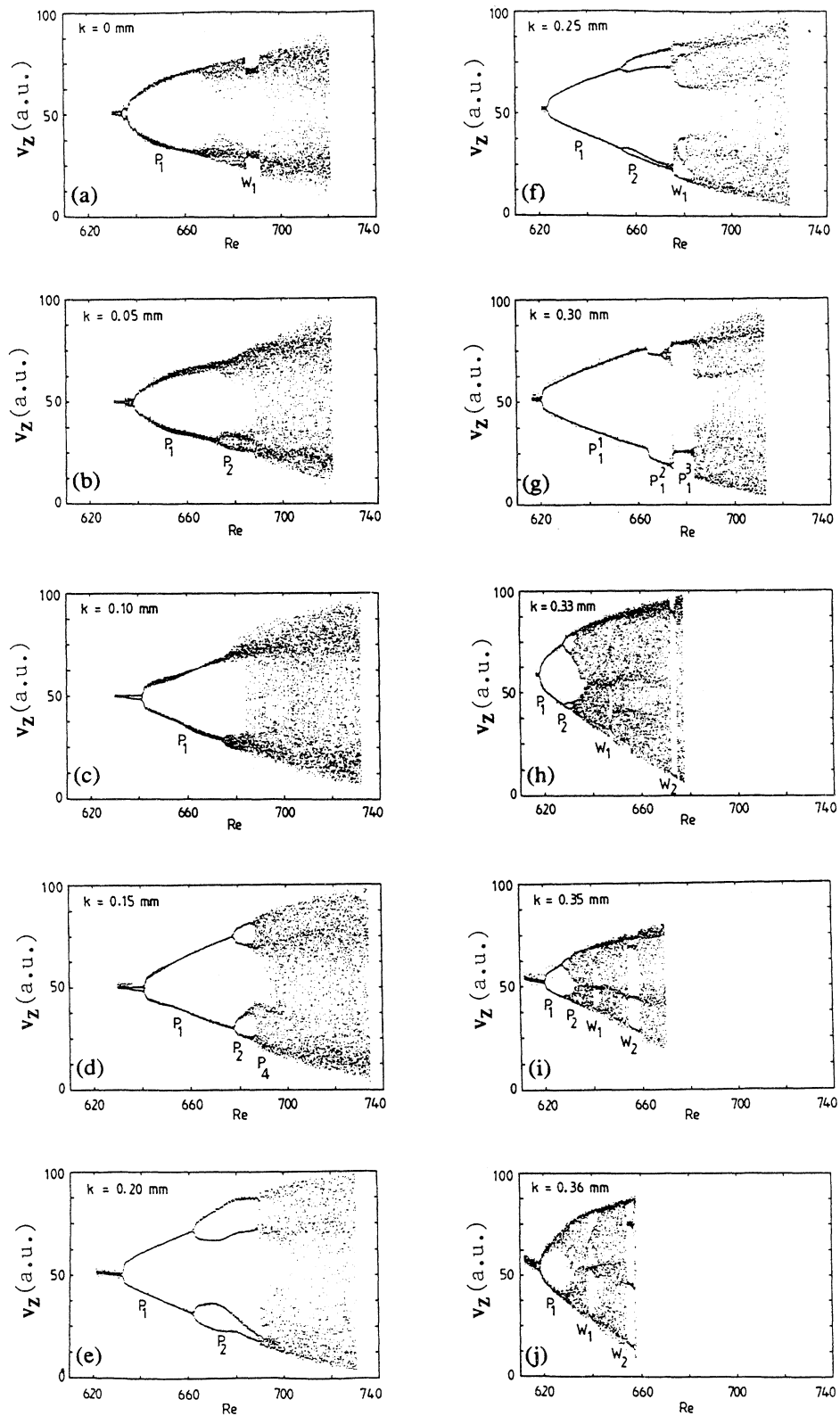
FIG. 4. Bifurcation diagrams obtained by plotting successive extrema of the axial velocity while the Reynolds number is ramped quasistatically. From (a) to (j) the inclination of the top plate is increased from $k = 0$ mm (0°) to $k = 0.36$ mm (0.42°).

TABLE I. Experimental scaling number δ^* obtained from the Taylor-Couette system.

k \ $\Gamma=$	0.330	0.335	0.355	0.360	0.362	0.365
0.10					2.35	6.00
0.13			2.11	2.00		4.67
0.23	6.00	3.67				
0.25	1.22	2.67				

where Re_j is the critical Reynolds number for the jth period-doubling bifurcation [19]. The values are obtained for different aspect ratios and inclination of the top plate. A comparison with the theoretical Feigenbaum number [20] of the simple logistic model, which is determined to be $\delta = 4.6992\ldots$, shows that the one-dimensional map is not sufficient to characterize the period-doubling sequences found in Taylor-Couette flow. On the other hand we have to calculate our scaling number δ^* from the limit of the finite cascade Re_j $(j \rightarrow j_{\max})$. In the present experiment we found a maximum of five $(j_{\max}=5)$ successive period doublings.

The observed scenarios are plotted in a Re-Γ diagram for $k=0.05$ mm (0.06°) in Fig. 5(a) and for $k=0.10$ mm (0.12°) in Fig. 5(b). Period multiples are indicated by a number reflecting the periodicity. Intermittencies are marked with (Im) and beats with (Schw). In addition, at period-doubling cascades (P) the largest observable periodicity is given. A rich variety of scenarios can be found which suggest the scenario of the standard logistic map. But this conjecture is not correct because the bifurcation diagrams are projections of a higher-dimensional system, as can be shown below when the dynamic variables such as fractal dimensions and Lyapunov exponents are estimated.

IV. METHODS

A variety of methods is available to characterize time series measured on nonlinear dynamical systems. One can calculate power spectra with fast-Fourier-transform (FFT) algorithms, and the corresponding autocorrelation function with the help of the Wiener-Khintchine theorem. Figure 6 shows the time series $v_z(t)$, the autocorrelation function $c(\tau)$, and the power spectrum of the axial velocity component. The left-hand column represents the state of the Taylor-Couette flow at Re$=701$, and the right-hand column at Re$=718$ [$\Gamma=0.374$, $k=0.2$ mm (0.23°)]. While the time series of both chaotic states look very similar, the autocorrelation function reveals the different system states. The $c(\tau)$ for Re$=718$ decays faster than for Re$=701$, as expected for a more chaotic state. The power spectra show more details. One sees broad spectra at low frequencies with different levels but the same main peak at $f_m \approx 0.7$ Hz. Besides this main peak one recognizes smaller peaks at $f_i = (i/5)f_m$ $(i=1,2,\ldots)$, corresponding to a quintupling in the inverse cascade. Unfortunately the efficiency of these methods is limited if one wants to give quantitative characterizations of different chaotic time series.

More detailed results are obtained with the powerful methods which we briefly describe on experimental examples below. To classify the time series one first reconstructs the phase space (or rather embedding space) of the nonlinear dynamical system. This is usually done with Takens's delay-time coordinates [21], where a vector in the embedding space is given by

$$\mathbf{x}(t_s) = (v_z(t_s), v_z(t_s+\tau), \ldots, v_z(t_s+\tau[d_E-1])) . \qquad (2)$$

$s = 1, \ldots, N_{\mathrm{dat}} - (d_E-1)\tau/T_a$; d_E is the embedding dimension, N_{dat} is the number of sampled data points, τ is the delay time, and T_a is the sampling time. For conven-
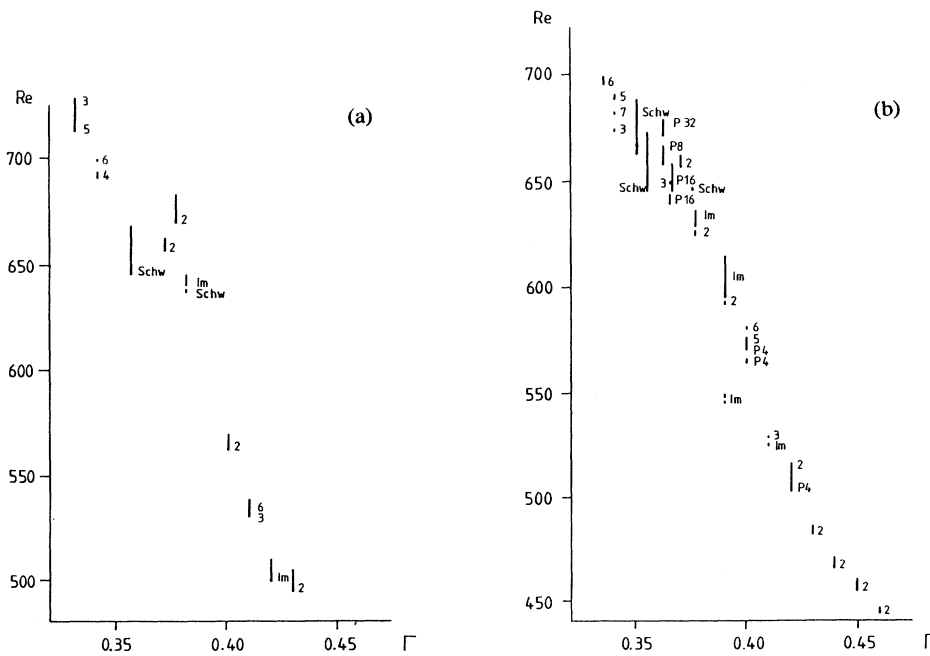

FIG. 5. Spectra of scenarios in the Γ-Re diagram. (a) $k=0.05$ mm (0.06°) and (b) $k=0.10$ mm (0.12°).
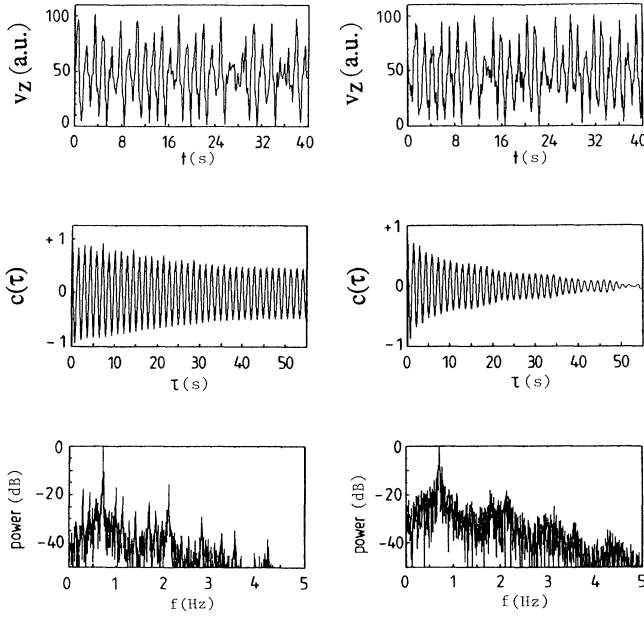
FIG. 6. Time series $v_z(t)$, autocorrelation function $c(\tau)$, and power spectrum for $\Gamma = 0.374$, $k = 0.20$ mm $(0.23°)$. Left-hand column: Re$=701$; right-hand column: Re$=718$.

ience we shall write x_s instead of $x(t_s)$.

To find optimal embedding parameters, i.e., the proper delay time τ and a sufficiently large embedding dimension d_E, one has to calculate the fill factor $f_{d_E}(\tau)$ (a measure of the utilization of the embedding space in any embedding dimension) or the integral local deformation $\Delta_{d_E}(\tau)$ (a measure of the homogeneity of the local flow).

The fill factor is defined by

$$f_{d_E}(\tau) \equiv \log_{10}\left[\frac{1}{N_{ref}} \frac{\sum_{k=1}^{N_{ref}} V_{d_E,k}(\tau)}{\langle V_{d_E} \rangle}\right], \qquad (3)$$

where $V_{d_E,k}(\tau)$ is the volume of the kth parallelepiped defined by (d_E+1) corner points which are arbitrarily distributed on the attractor, $\langle V_{d_E} \rangle$ is a normalization by the volume which covers the attractor in each embedding dimension d_E, and N_{ref} is the number of reference points. The first maxima of the fill factor, corresponding to maximum spanned attractors in the embedding space, provide proper delay times. A sufficiently large embedding dimension can be obtained by the convergency of the qualitative structure of the fill factor for successively increasing embedding dimension. A detailed description of this method can be found in [22,23].

To define the integral local deformation $\Delta_{d_E}(\tau)$ one calculates the evolution of successive distances between a reference point and the center of mass of neighboring points when time proceeds. In an optimal reconstruction, for which we require homogeneity of the local flow, points on neighboring trajectories remain neighboring for

small evolution times. The first minima of $\Delta_{d_E}(\tau)$, corresponding to a maximum homogeneity of the local flow, provide proper delay times; the embedding dimension can be obtained from the convergency at these minima. For details see [23].

Figure 7(a) illustrates the fill factor for the Re$=701$ state discussed above. We calculated $f_{d_E}(\tau)$ for embedding dimensions $d_E = 2-10$ and delay times $\tau/T_c = 0-1.1$ (T_c is the period of the main frequency in the power spectrum shown in Fig. 6). The arrows A and B indicate proper delay times. Figure 7(b) shows the integral local deformation in the same interval as the fill factor. $\Delta_{d_E}(\tau)$ is normalized by (τ/T_a), which is often convenient for chaotic time series [23,24]. Arrows A and B again indicate proper delay times at minima. The result of this calculation is the same as the result obtained from the fill factor, i.e., the local flow is homogeneous when the attractor is maximally spanned. An estimate of the sufficiently large embedding dimension yields $d_E = 7$.

In Fig. 8 one sees the reconstructions of the strange attractors, which correspond to the states introduced in
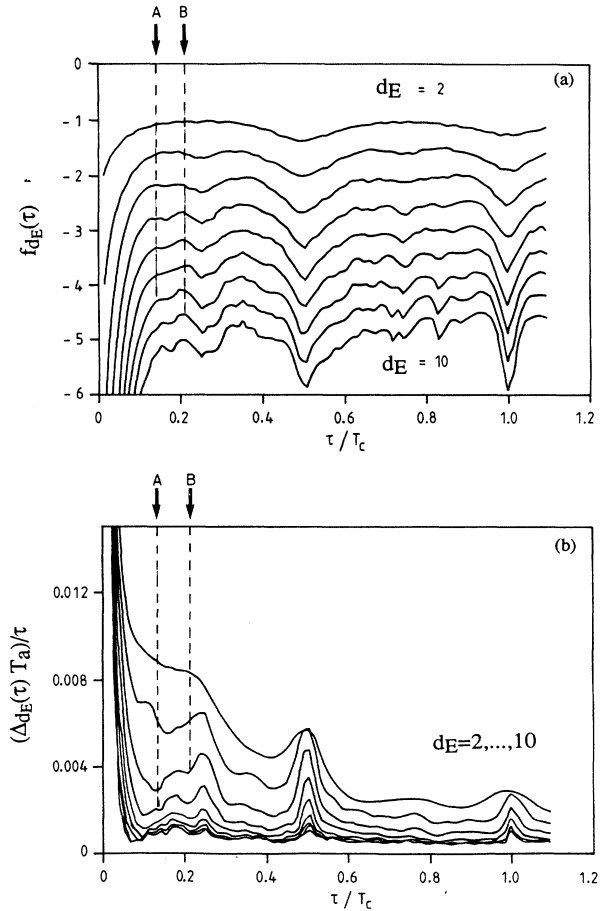

FIG. 7. Fill factor and averaged integral local deformation vs normalized delay time for embedding dimensions $d_E = 2-10$ [$\Gamma = 0.374$, $k = 0.20$ mm $(0.23°)$, Re$=701$]. Proper values for the delay time are indicated by dashed lines at arrows A and B.
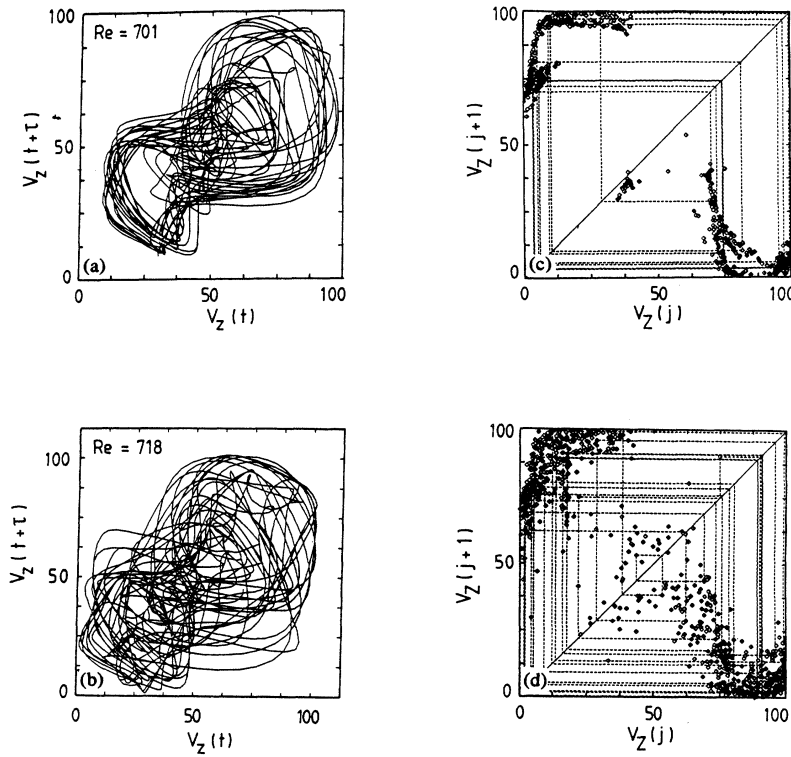
FIG. 8. (a) and (b) Reconstructions of the strange attractors with delay time coordinates. (c) and (d) Corresponding return maps.

Fig. 6, with delay times $\tau/T_c \approx 0.22$ (indicated with arrow B in Fig. 7 for Re = 701). On the right-hand side the corresponding return maps are given. We took the extreme values of the velocity time series, i.e., successive minima and maxima, as $v_z(j)$. The return map was reconstructed by plotting $v_z(j)$ vs $v_z(j+1)$. In Fig. 8(c) all points lie on a complex curve with some variance, indicating that this flow shows deterministic chaos having a strange attractor. The dotted lines show a few iterations on the attractor. In Fig. 8(d), the corresponding return map of the Re = 718 state looks more complicated than Fig. 8(c) and it is hard to decide whether one sees an attractor or noise-dominated dynamics.

To indicate a low-dimensional strange attractor in cases where the fill factor or the integral local deformation show no clear results for a sufficiently large embedding dimension, one usually calculates the dynamic variables such as fractal dimensions, Lyapunov spectra, or entropies for increasing embedding dimensions, looking for a convergence of these values.

To estimate the fractal dimension of the reconstructed strange attractors in phase space we calculate the correlation dimension D_2 [25]

$$C(R) \propto R^{D_2} \rightarrow D_2 = \lim_{R \to 0} \frac{\log_{10}(C(R))}{\log_{10}(R)} . \qquad (4)$$

R is the scaling radius and $C(R)$ is the correlation integral

$$C(R) \approx \frac{1}{N_{\text{ref}}} \sum_{j=1}^{N_{\text{ref}}} \frac{1}{N_{\text{dat}}} \sum_{i=1}^{N_{\text{dat}}} \sigma(R - \|x_i - x_j\|) , \qquad (5)$$

where σ is the Heaviside function, N_{dat} is the number of points in phase space, and N_{ref} is a sufficiently large number of reference points.

Figure 9 illustrates the results obtained from the experimental attractors introduced above. In Fig. 9(a) the double-logarithmic plot of the correlation integral versus radius is shown for the Re = 701 state, and in Fig. 9(b) for the Re = 718 state. The radius is given in percent of the global attractor extension. Both attractors contain $N_{\text{dat}} = 32\,768$ data points in the resolution of a 12-bit ADC. We chose $N_{\text{ref}} = 3000$ reference points for an estimate of the correlation integral. In the plots $C(R)$ is drawn for embedding dimensions $d_E = 1-12$. The dashed lines illustrate the fit of the slopes yielding the correlation dimension D_2. For Re = 701 one obtains $D_2 \approx 2.45 \pm 0.15$; for Re = 718, $D_2 \approx 4.2 \pm 0.2$. Obviously one cannot perform the required limit $R \rightarrow 0$ for the dimension calculation, because due to noise one finds a "knee" in the double-logarithmic $C(R)$ plots at approximately $R = 2\%$. Below that value the trajectories tend to fill the embedding space in any dimension, leading to a correlation dimension $D_2 = d_E$. Above this knee the fractal geometry of the strange attractor can be detected. Figure 9(c) shows the convergency of the slopes versus embedding dimension. From $d_E > 6$ the value of D_2 converges for the Re = 701 state. This is the result which we predicted with the integral local deformation in Fig. 7(b).

The sequence of Figs. 10(a)–10(f) shows the dynamic behavior of points on the experimental strange attractor (Re = 714, $\Gamma = 0.374$, $k = 0.2$ mm). Starting with an initial spherical cloud of points it can be recognized that

due to the chaotic dynamics these points separate from each other. After an evolution time $t_{ev} \approx 0.44 T_c$ the initial sphere becomes an ellipsoid. This is the characteristic "stretching" process known as the butterfly effect, i.e., the system shows sensitivity to small variations of initial conditions. Due to dissipation, volume elements in the embedding space shrink. It can be seen in Fig. 10(b) that although we find expansion in one direction other directions may shrink. Additionally, because of a finite boundary of the attractive basin, the ellipsoid must be folded. This folding process can be observed in Figs. 10(c) and 10(d). For evolution times $t_{ev} > 2 T_c$, points

from the initial sphere are distributed over the entire attractor [Figs. 10(e) and 10(f)]. This stretching, shrinking, and folding process leads to a very complicated self-similar structure of the strange attractor which we measured with the correlation dimension. To measure the dynamic behavior, i.e., the averaged time constants for the stretching and shrinking processes, one estimates the Lyapunov exponents λ_k. We usually approximate the linearized flow map T_j by a least-squares fit [26,27] and obtain the spectrum of Lyapunov exponents from

$$\lambda_k = \lim_{t_{ev} \to \infty} \frac{1}{t_{ev}} \log_2 \| T_{j_{t_{ev}}} e_j^k \| , \qquad (6)$$

where e_j^k $(k = 1, \ldots, d_E)$ is an orthonormal base and t_{ev} is the evolution time. Implementation details of this linear fit are described in [28]. Figure 11(a) shows the spectrum of Lyapunov exponents versus embedding dimension for the Re=701 state, and Fig. 11(b) for the Re=718 state. The dotted lines indicate the estimated exponents averaged from the values marked with solid squares for higher embedding dimensions. While for Fig.
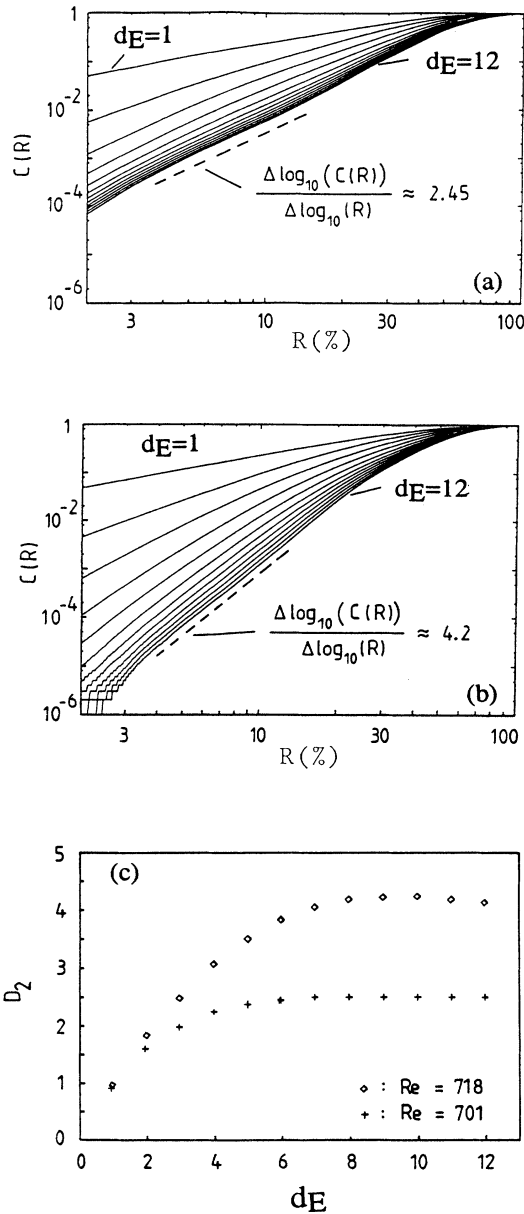

FIG. 9. Double-logarithmic plotted correlation integrals $C(R)$ vs scaling radius R from $d_E = 1-12$. (a) Re=701, (b) Re=718, (c) convergence of D_2.
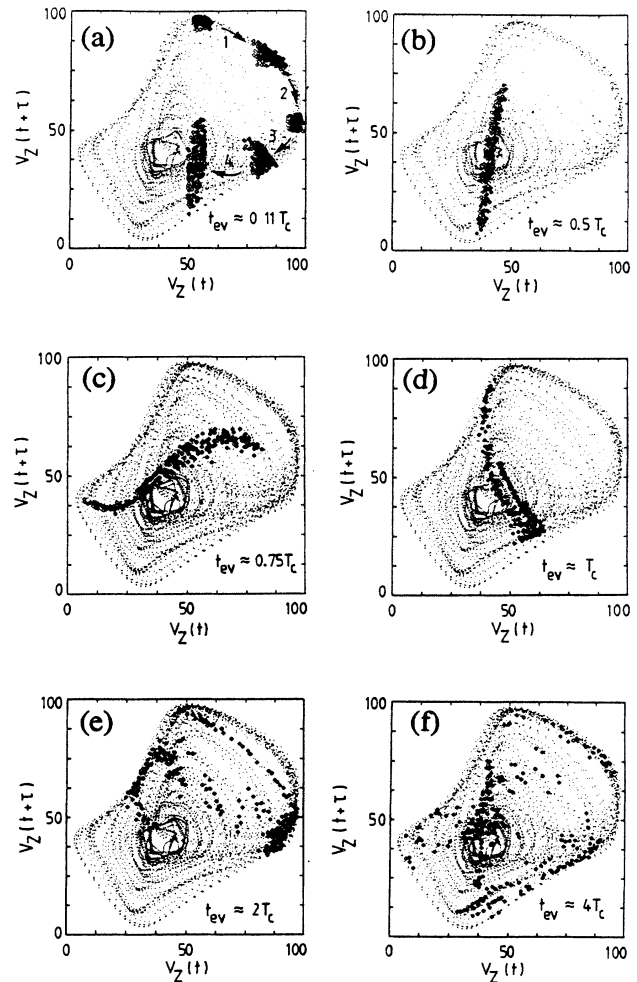

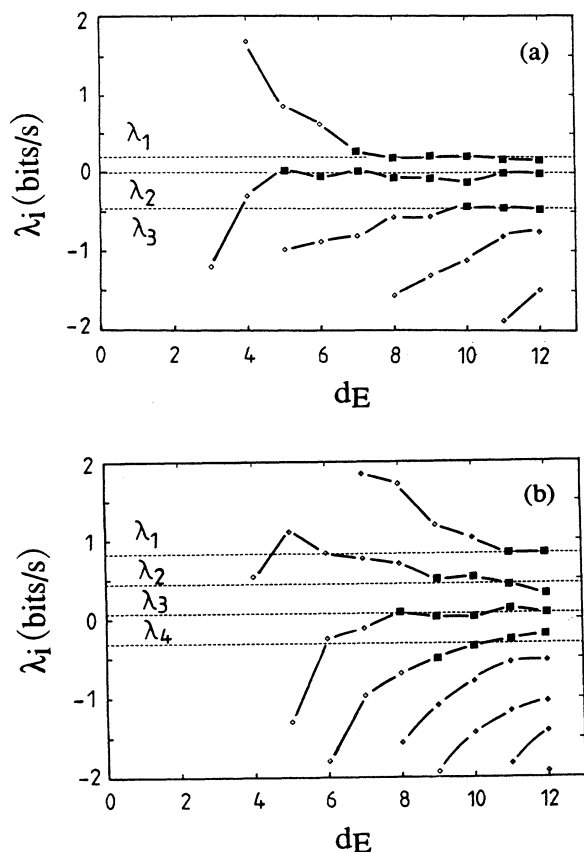FIG. 10. "Stretching and folding": Evaluation of an initial sphere on an experimental strange attractor.

FIG. 11. Spectra of Lyapunov exponents vs Reynolds number. (a) Re=701, (b) Re=718. The dotted lines indicate the averaged values obtained from the bold squares.

11(a) the spectrum $(\lambda_1, \lambda_2, \lambda_3) \approx (0.32, 0, -0.59)$ bits/orbit is complete, the spectrum from Fig. 11(b), $(\lambda_1, \lambda_2, \lambda_3, \lambda_4) \approx (1.58, 0.75, 0.06, -0.36)$ bits/orbit, cannot be complete, because the sum of the exponents must be negative for dissipative systems. If we try to use the reversal of the time series we may obtain more information about the negative Lyapunov exponents [29]. A very rough estimation yields $(\lambda_5, \lambda_6) \approx (-0.99, -1.85)$ bits/orbit.

From the spectrum of Lyapunov exponents one calculates the Kaplan-Yorke dimension D_{KY} using the conjecture [30]

$$D_{KY} \equiv j + \frac{\sum_{k=1}^{j} \lambda_k}{|\lambda_{j+1}|} ,$$

where   (7)

$$\sum_{k=1}^{d_E} \lambda_k < 0, \quad \sum_{k=1}^{j} \lambda_k \geq 0, \quad \text{and} \sum_{k=1}^{j+1} \lambda_k < 0 .$$

We find $D_{KY} \approx 2.53$ for Re=701 and $D_{KY} \approx 5.55$ for Re=718. Due to the uncertainty of the negative exponents, $D_{KY} \approx 5.55$ does not agree with the value of the

fractal dimension which we obtained with the correlation dimension D_2.

An essential measure of the chaoticity of a system's state is the entropy, which can be estimated from the Lyapunov exponents as the metric entropy

$$h = \sum_k \lambda_k^+ \tag{8}$$

for homogeneous attractors [31]. λ^+ denotes the positive exponents. The correlation entropy or order-2 Kolmogorov entropy [32] is given by

$$K_2 = - \lim_{d_E \to \infty} \lim_{\tau \to 0} (1/\tau) \log_2(P_{d_E}(\tau)) ,$$

where   (9)

$$P_{d_E}(\tau) \equiv \frac{C_{d_E+1}(\tau)}{C_{d_E}(\tau)} .$$

C_d is the correlation integral in the d_E-dimensional embedding space. Figure 12(a) shows plots of the logarithm of the ratio of successive correlation integrals versus normalized delay time, and illustrates how K_2 can be estimated from the slope at the accumulation line for higher d_E (dashed line) [24]. The convergence of K_2 versus embedding dimension is shown in Fig. 12(b). We averaged the K_2 values indicated as solid circles. For
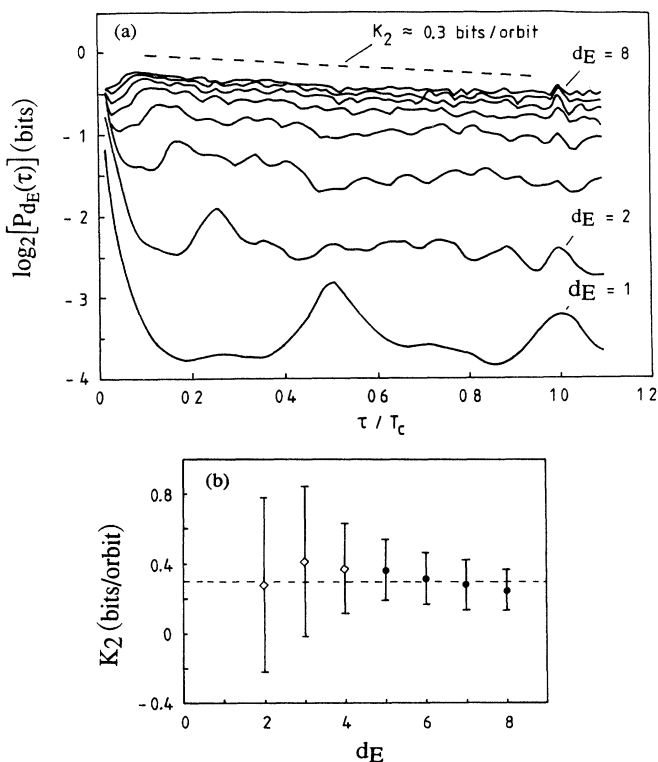

FIG. 12. (a) Estimate of the order-2 Kolmogorov entropy from the accumulation line of the logarithmic plotted successive correlation integrals for higher embedding dimensions. (b) Convergence of K_2 for increasing embedding dimension [$\Gamma = 0.374$, $k = 0.20$ mm (0.23°), Re=701].

Re = 701 the obtained value is $K_2 \approx 0.3$ bits/orbit, which fits to the value of the metric entropy [dashed line in Fig. 12(b)].

V. RESULTS OBTAINED FROM THE EXPERIMENTAL PERIOD-DOUBLING SCENARIOS IN TAYLOR-COUETTE FLOW

The calculated results for the fractal dimensions, Lyapunov exponents, and entropies are of little significance when they are not discussed as a function of the Reynolds number or the boundary conditions of the experiment. We will show that the evolution of these dynamic variables gives a useful quantitative characterization of the considered routes to chaos.

Figures 13(a)–13(d) illustrate the evolution of the dynamic variables for $\Gamma = 0.374$ and $k = 0.20$ mm (0.23°) in the Reynolds-number interval Re = 640–740. Figure 13(a) shows the evolution of the correlation dimension D_2 versus Reynolds number. From Re ≈ 633 to 663 one finds a period-1 mode. At Re ≈ 663 a period-doubling bifurcation appears, leading to a period-2 mode, and at Re ≈ 691 the transition to chaos occurs. From Re ≈ 633 to Re$_c \approx 691$ the estimated correlation dimension is $D_2 \approx 1$ as expected. For increasing values of Reynolds number the value of D_2 increases. We found a transition to chaos following $D_2 \propto (\text{Re} - \text{Re}_c)^{1/4}$, which is very similar to a continuous phase transition. At Re ≈ 730 the chaotic dy-

namics of the symmetric s_1^* flow becomes globally unstable and the asymmetric oscillatory one-vortex flow a_1 is established. The values for the dimension grow up to $D_2 \approx 4.3$ in the end of the chaotic regime, which is a clear indication that this bifurcation sequence cannot be simulated by a simple low-dimensional map such as the logistic map, when we interpret D_2 as a lower estimate of the system's degrees of freedom. The error bars in this plot correspond to the standard deviation of the averaging process over higher embedding dimensions and to the standard deviation of the linear regression when D_2 is determined from the slope of the double-logarithmic correlation integral.

Figure 13(b) shows the evolution of the Lyapunov spectrum versus Reynolds number in the same interval. Positive Lyapunov exponents indicate chaotic motion. The onset of chaos is found at Re$_c \approx 691$. For higher Reynolds numbers we estimate up to six exponents, keeping in mind that the accuracy for negative exponents is not very high due to a tangential space which is not well spanned in the stable directions, leading to poor statistics. The uncertainty is at least $\Delta\lambda = \pm 0.5$ bits/orbit.

So the absolute values of the exponents are not very useful but again the evolution, the relative behavior of λ_i when the Reynolds number is varied, is very interesting. The positive values show the same trend as D_2, i.e., a strong increase in the beginning of the chaotic regime and a slower increase in the end of the stable s_1^* branch.
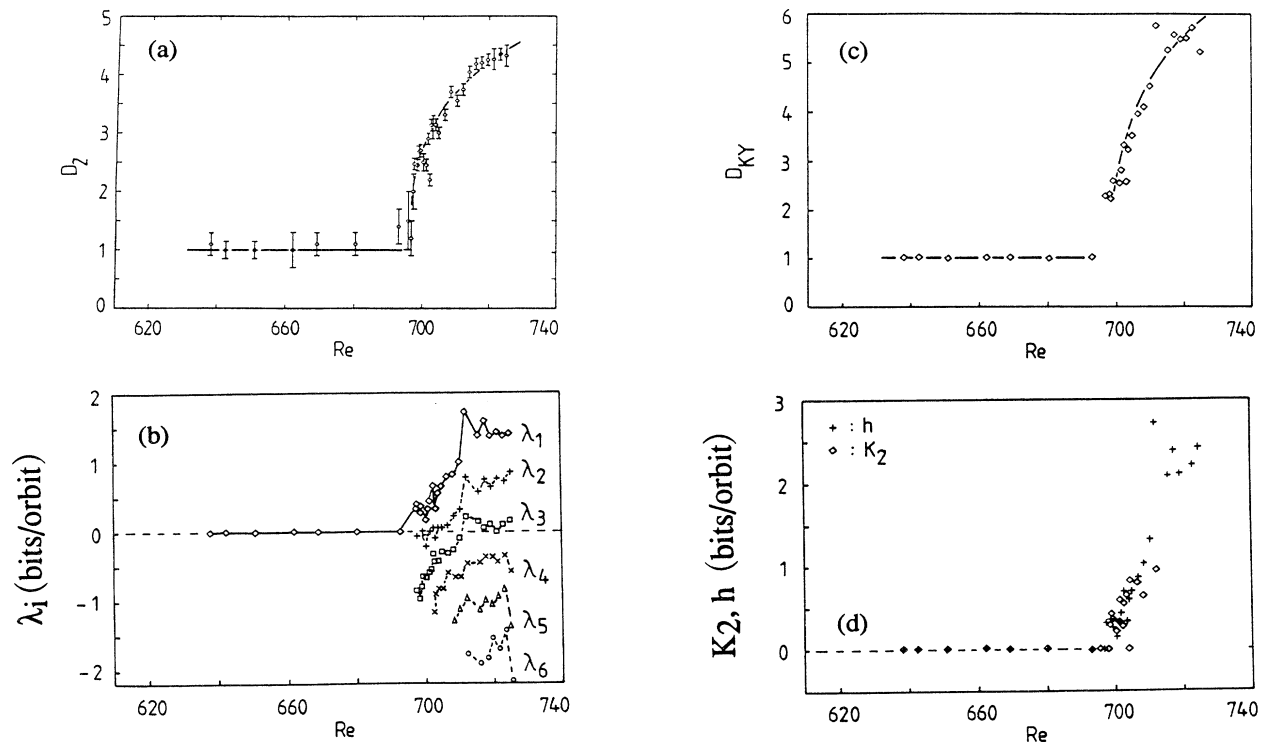

FIG. 13. (a) Evolution of the correlation dimension as a function of Reynolds number, (b) spectra of Lyapunov exponents vs Reynolds number, (c) Kaplan-Yorke dimension vs Reynolds number, and (d) entropies vs Reynolds number for $\Gamma = 0.374$ and $k = 0.20$ mm (0.23°).

The evolution of the Kaplan-Yorke or Lyapunov dimension is illustrated in Fig. 13(c). D_{KY} shows a smooth nonlinear increase as a function of the Reynolds number. To help visualize this we plot $D_{KY} \propto (\text{Re} - \text{Re}_c)^{1/4}$. One has to take into account that due to the connection to the Lyapunov spectra the errors of these values are larger than the errors for D_2.

From the spectrum of Lyapunov exponents one can calculate the metric entropy h, indicated with crosses in Fig. 13(d). The diamonds show the values of the order-2 Kolmogorov entropy K_2. We calculated K_2 only in the low-dimensional regime $\text{Re} \approx 630-715$. For the higher-dimensional data the statistics become insufficient. Here the transition to chaos is described by an entropy increasing linearly.

An open question is whether the behavior of the dynamic variables of a period doubling into chaos, as described above, can be a paradigm for all period-doubling scenarios. We cannot give an answer in this paper, but we will give a hint that this is not improbable. A second scenario is investigated for $\Gamma = 0.374$ and $k = 0.33$ mm (0.38°). Figure 14 shows the bifurcation diagram corresponding to Fig. 4(h). In Fig. 14(a) one period doubling (from P_1 to P_2) is observable. An extension of the regime at the accumulation point ($\text{Re}_c \approx 633$) of the period-doubling cascade reveals a period-4 (P_4) [Fig. 14(b)]. Figures 14(c) and 14(d) show two extensions of the first visible periodic window W_1, illustrating a noisy period doubling. In the extension of the second periodic window W_2 [Fig. 14(e)] a similar scenario can be seen.
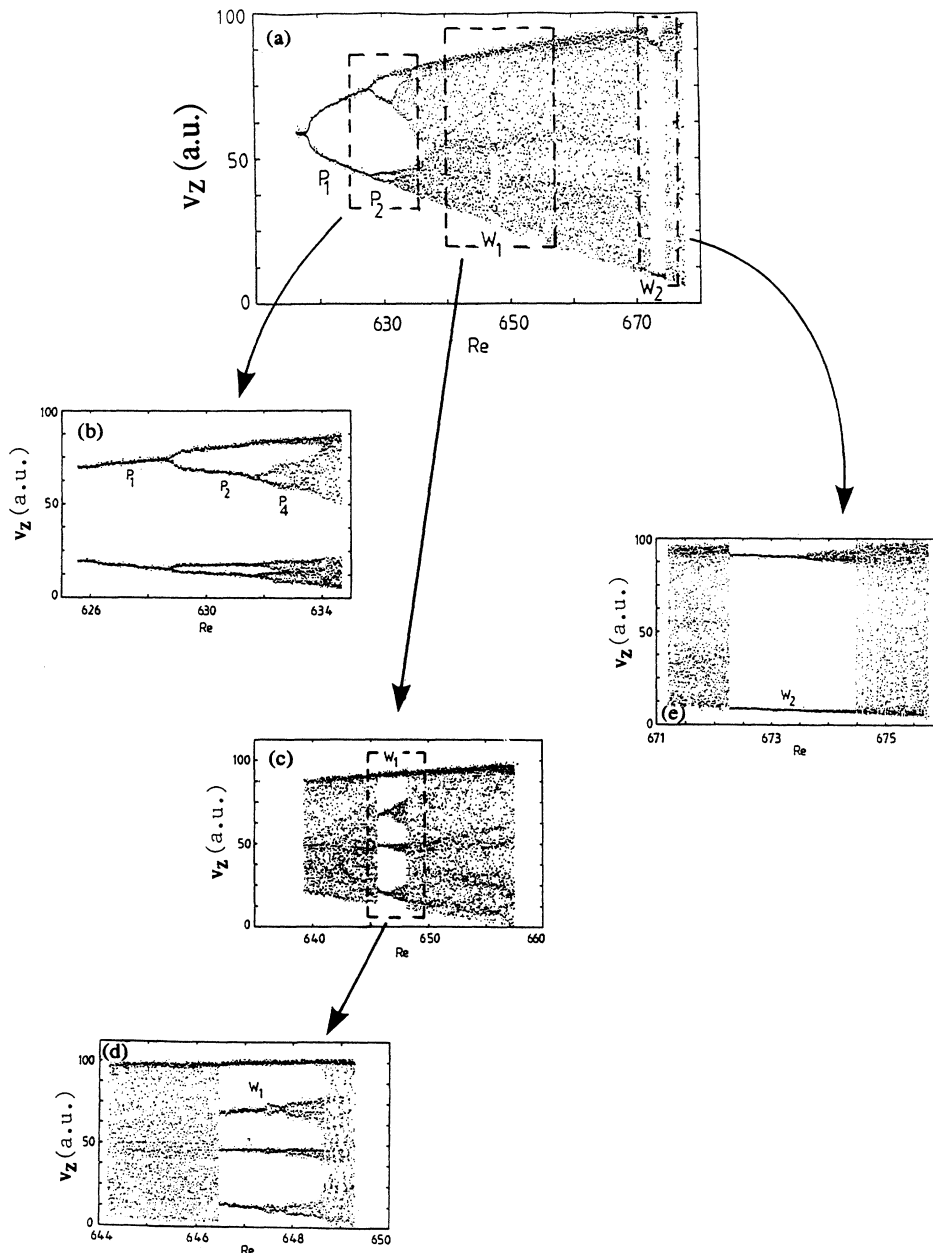

FIG. 14. (a) Bifurcation diagram for $\Gamma = 0.374$ and $k = 0.33$ mm (0.38°), (b) expansion of the accumulation point, (c) and (d) expansion of the first periodic window W_1, (e) expansion of the second periodic window W_2.
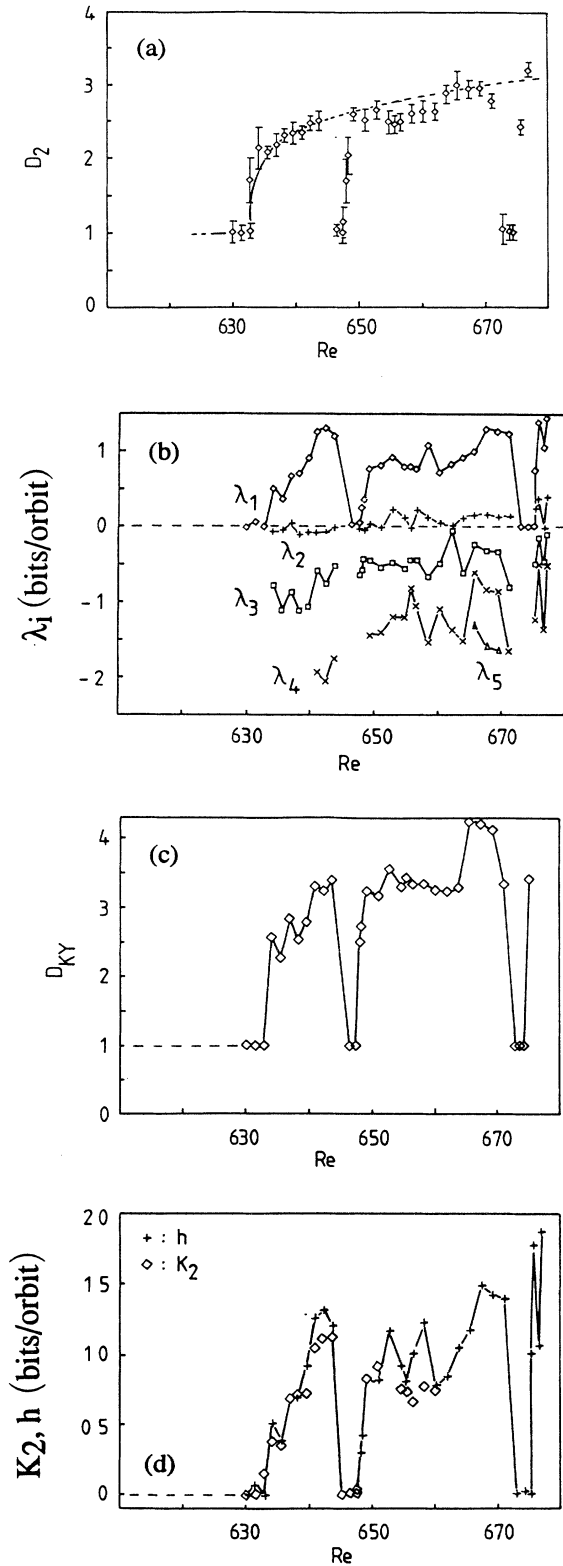
FIG. 15. (a) Evaluation of the correlation dimension as a function of Reynolds number, (b) spectra of Lyapunov exponents vs Reynolds number, (c) Kaplan-Yorke dimension vs Reynolds number, and (d) entropies vs Reynolds number for $\Gamma = 0.374$ and $k = 0.33$ mm $(0.38°)$.

We are interested again in the evolution of the dynamic variable of this sequence to chaos. Figure 15(a) shows the correlation dimension D_2 versus Reynolds number. One finds a behavior of D_2 similar to the bifurcation discussed above. The curve $D_2 \propto (\mathrm{Re} - \mathrm{Re}_c)^{1/4}$ is drawn in this diagram. In the periodic windows D_2 is found to be 1. The spectra of Lyapunov exponents are given in Fig. 15(b). The trend of the first Lyapunov exponent (λ_1, indicated with diamonds) corresponds to the evolution of D_2. The second exponent is approximately zero for nearly the whole scenario [we think that deviations from zero are due to noise, in contrast to the second exponent in Fig. 13(b)]. For the periodic windows we cannot estimate negative Lyapunov exponents using the approximation of the tangential map because the tangential space is not spanned in all relevant directions. The Kaplan-Yorke dimension drawn in Fig. 15(c) as well as the metric and correlation entropy in Fig. 15(d) also reflect the trend suggested by the correlation dimension.

Recent optimistic estimates show that a value of $D_2 \approx 4.3$ for a data set containing $N_{\mathrm{dat}} = 32\,768$ points is reliable [33]. Proof (not in a mathematical sense but more from an experimentalist's point of view) that the obtained value for D_2 actually represents the underlying dynamics can be given by showing the evolution of the correlation dimension for a variation of the control parameter. From this procedure one finds an answer to the question of spurious correlation dimensions due to a convergency of the slopes of the double-logarithmic plotted correlation integrals for a small number of data points or colored noise. Otherwise, much effort is necessary to detect these effects [34,35].

The same situation exists with regard to the spectra of Lyapunov exponents. Strong efforts have been made to identify true and spurious Lyapunov exponents when the embedding dimension is larger than the number of relevant degrees of freedom. An estimate of the sufficiently large embedding dimension with the fill factor or the integral local deformation gives the correct embedding dimension only for the Euclidean embedding, not for the original phase space, and is of no help concerning this problem. Calculating the evolution of the Lyapunov spectra in addition to the evolution of the spectra of the time-reversed attractor for a variation of the control parameters simplifies the identification of exponents of physical relevance. A comparison of the corresponding Kaplan-Yorke dimension with the correlation dimension verifies the results.

VI. CONCLUSION

We estimated the dynamic variables such as fractal dimensions, Lyapunov exponents, and entropies not only for a few attractors measured from sequences into chaos, but also showed the evaluation of these variables when the control parameters of the experiment are varied. The efforts of measuring and interpreting many (> 50) time series are justified by the results of this procedure.

We found a remarkable functional dependence of the fractal dimension on the Reynolds number for the investigated period-doubling routes. The curve $D_2 \propto (\mathrm{Re} - \mathrm{Re}_c)^{1/4}$ shows that the transition from period-

ic to chaotic dynamics is similar to continuous phase transitions, and D_2 is a sufficient order parameter in this case. The other dynamic variables show the same trend as the correlation dimension, but are more sensitive to measurement noise which is not negligible for real physical systems. The work on noise-reduction methods is in progress and will be published elsewhere [36].

[1] A. Brandstäter and H. L. Swinney, Phys. Rev. A **35**, 2207 (1987).

[2] G. Pfister, in *Flow of Real Fluids,* edited by G. E. A. Meier and F. Obermeier, Lecture Notes in Physics Vol. 235 (Springer, Berlin, 1985), p. 199.

[3] T. Mullin and K. A. Cliffe, in *Nonlinear Phenomena and Chaos,* edited by S. Sarkar (Hilger, Bristol, 1986), p. 96.

[4] A. Brandstäter, J. Swift, H. L. Swinney, A. Wolf, J. D. Farmer, E. Jen, and J. P. Crutchfield, Phys. Rev. Lett. **51**, 1442 (1983).

[5] T. Mullin, K. A. Cliffe, and G. Pfister, Phys. Rev. Lett. **58**, 2212 (1987).

[6] T. Mullin, IMA J. Appl. Math. **46**, 109 (1991).

[7] G. Pfister, Th. Buzug, and N. Enge, Physica D **58**, 441 (1992).

[8] Th. Buzug, J. von Stamm, and G. Pfister, Physica A **191**, 559 (1992).

[9] G. Ahlers and D. S. Cannell, in *Synergetics—From Microscopic to Macroscopic Order,* edited by E. Frehland and H. Haken (Springer-Verlag, New York, 1983).

[10] R. C. Di Prima and H. L. Swinney, in *Hydrodynamic Instabilities and Transition to Turbulence,* edited by H. L. Swinney and J. P. Gollub (Springer-Verlag, New York, 1980), p. 128.

[11] T. B. Benjamin and T. Mullin, J. Fluid Mech. **121**, 219 (1982).

[12] G. Pfister, H. Schmidt, K. A. Cliffe, and T. Mullin, J. Fluid Mech. **191**, 1 (1988).

[13] G. Pfister, in *Laser Anemometry in Fluid Mechanics,* edited by D. F. G. Durao (Ladoan, Portugal, 1984), p. 159.

[14] A. Libchaber and J. Maurer, in *Nonlinear Phenomena at Phase Transitions and Instabilities,* edited by T. Riste (Plenum, New York, 1981), p. 259.

[15] M. Giglio, S. Musazzi, and U. Perini, in *Nonlinear Phenomena at Phase Transitions and Instabilities* (Ref. [14]), p. 287.

[16] P. S. Lindsay, Phys. Rev. Lett. **47**, 1349 (1981).

[17] A. Schulz, Diplomarbeit, Christian-Albrechts-Universität zu Kiel, 1988.

[18] G. Pfister, U. Gerdts, A. Lorenzen, and K. Schätzel, in *Photon Correlating Techniques in Fluid Mechanics,* edited by O. Schulz-Dubois, Springer Series in Optical Science Vol. 38 (Springer, New York, 1983), p. 256.

[19] G. Geister, Diplomarbeit, Christian-Albrechts-Universität zu Kiel, 1985.

[20] M. J. Feigenbaum, Los Alamos Sci. **1**, 4 (1980).

[21] F. Takens, in *Dynamical Systems and Turbulence,* edited by D. A. Rand and L.-S. Young, Lecture Notes in Mathematics Vol. 898 (Springer, Berlin, 1980), p. 230.

[22] Th. Buzug, T. Reimers, and G. Pfister, Europhys. Lett. **13**, 605 (1990).

[23] Th. Buzug and G. Pfister, Phys. Rev. A **45**, 7073 (1992).

[24] Th. Buzug and G. Pfister, Physica D **58**, 127 (1992).

[25] P. Grassberger and I. Procaccia, Physica D **9**, 189 (1983).

[26] J.-P. Eckmann, S. O. Kamphorst, D. Ruelle, and S. Ciliberto, Phys. Rev. A **34**, 4971 (1986).

[27] M. Sano and Y. Sawada, Phys. Rev. Lett. **55**, 1082 (1985).

[28] Th. Buzug, T. Reimers, and G. Pfister, in *Nonlinear Evolution of Spatio-Temporal Structures in Dissipative Continuous Systems,* edited by F. H. Busse and L. Kramer (Plenum, New York, 1990), p. 7.

[29] U. Parlitz, Int. J. Bifurc. Chaos **1**, 155 (1992).

[30] P. Frederickson, J. L. Kaplan, E. D. Yorke, and J. A. Yorke, J. Differ. Equations **49**, 185 (1983).

[31] H. G. Schuster, *Deterministic Chaos,* 2nd ed. (VCH-Verlag, Weinheim, 1988).

[32] J. G. Caputo and P. Atten, Phys. Rev. A **35**, 1311 (1987).

[33] J.-P. Eckmann and D. Ruelle, Physica D **56**, 185 (1992).

[34] J. Theiler, S. Eubank, A. Longtin, B. Galdrikian, and J. D. Farmer, Physica D **58**, 77 (1992).

[35] M. Dämmig, C. Boden, and F. Mitschke, Appl. Phys. B **55**, 121 (1992).

[36] N. Enge, Th. Buzug, and G. Pfister (unpublished).